

Statistical analysis of wave propagation properties of equatorial noise observed at low altitudes

Miroslav Hanzelka¹, Frantisek Nemec², Ondrej Santolik³, and Michel Parrot⁴

¹Institute of Atmospheric Physics (CAS)

²Charles University

³Department of Space Physics, Institute of Atmospheric Physics of the Czech Academy of Sciences

⁴LPC2E/CNRS, Orleans, France

November 22, 2022

Abstract

Equatorial noise is an electromagnetic emission with line spectral structure, predominantly located in the vicinity of the geomagnetic equatorial plane at radial distances ranging from 2 to 8 Earth's radii. Here we focus on the rare events of equatorial noise occurring at ionospheric altitudes during periods of strongly increased geomagnetic activity. We use multicomponent electromagnetic measurements from the entire 2004–2010 DEMETER spacecraft mission and present a statistical analysis of wave propagation properties. We show that, close to the Earth, these emissions experience a larger spread in latitudes than they would at large radial distances and that their wave normals can significantly deviate from the direction perpendicular to local magnetic field lines. These results are compared to ray tracing simulations, in which whistler mode rays with initially nearly perpendicular wave vectors propagate down to the low altitudes with wave properties corresponding to the observations. We perform nonlinear fitting of the simulated latitudinal distribution of incident rays to the observed occurrence and estimate the distribution of wave normal angles in the source. The assumed Gaussian distribution provides the best fit with a standard deviation of 2° from the perpendicular direction. Ray tracing analysis further shows that small initial deviations from the meridional plane can rapidly increase during the propagation and result in deflection of the emissions before they can reach the altitudes of DEMETER.

Statistical analysis of wave propagation properties of equatorial noise observed at low altitudes

Miroslav Hanzelka^{1,2}, František Němec², Ondřej Santolík^{1,2}, Michel Parrot³

¹Department of Space Physics, Institute of Atmospheric Physics of the Czech Academy of Sciences,
Prague, Czech Republic

²Faculty of Mathematics and Physics, Charles University, Prague, Czech Republic

³LPC2E/CNRS, Orléans, France

Key Points:

- We present statistical analysis of wave propagation properties of equatorial noise observed at low altitudes by the DEMETER spacecraft
- The wave propagation properties are explained by 3D ray tracing simulations in a cold plasma
- Comparison of the spacecraft observations and ray statistics suggests a narrow distribution of wave normal angles in the source

Corresponding author: M. Hanzelka, mha@ufa.cas.cz

15 **Abstract**

16 Equatorial noise is an electromagnetic emission with line spectral structure, predomi-
 17 nantly located in the vicinity of the geomagnetic equatorial plane at radial distances rang-
 18 ing from 2 to 8 Earth’s radii. Here we focus on the rare events of equatorial noise oc-
 19 ccurring at ionospheric altitudes during periods of strongly increased geomagnetic activ-
 20 ity. We use multicomponent electromagnetic measurements from the entire 2004–2010
 21 DEMETER spacecraft mission and present a statistical analysis of wave propagation prop-
 22 erties. We show that, close to the Earth, these emissions experience a larger spread in
 23 latitudes than they would at large radial distances and that their wave normals can sig-
 24 nificantly deviate from the direction perpendicular to local magnetic field lines. These
 25 results are compared to ray tracing simulations, in which whistler mode rays with ini-
 26 tially nearly perpendicular wave vectors propagate down to the low altitudes with wave
 27 properties corresponding to the observations. We perform nonlinear fitting of the sim-
 28 ulated latitudinal distribution of incident rays to the observed occurrence and estimate
 29 the distribution of wave normal angles in the source. The assumed Gaussian distribu-
 30 tion provides the best fit with a standard deviation of 2° from the perpendicular direc-
 31 tion. Ray tracing analysis further shows that small initial deviations from the meridional
 32 plane can rapidly increase during the propagation and result in deflection of the emis-
 33 sions before they can reach the altitudes of DEMETER.

34 **Plain Language Summary**

35 We study the electromagnetic emission called equatorial noise, which occurs fre-
 36 quently in the magnetosphere of Earth and is known to have an impact on the radiation
 37 belt dynamics. Here we present statistics of the rare events when the emissions reached
 38 the altitudes of 700 km and were detected by the low orbiting satellite DEMETER. Our
 39 analysis reveals an unusually high spread of recorded events in the latitude, and we also
 40 notice large deviations of the wave vector from the perpendicular direction. The observed
 41 wave properties and indices of geomagnetic activity are used to set up a ray tracing sim-
 42 ulation. We confirm that the observations agree with the theoretical propagation prop-
 43 erties of rays in the whistler mode, which is the wave mode associated with equatorial
 44 noise. The correspondence between simulation and observation is further improved by
 45 inferring the initial wave properties in the source with the help of nonlinear least-squares
 46 fitting. Additional simulations of ray propagation with nonzero initial deviation from the

47 plane of local meridian confirm that such deviations must be minimal; otherwise, the rays
 48 become deflected before reaching the altitude of the DEMETER satellite.

49 **1 Introduction**

50 Equatorial noise (EN) is one of the most intense natural electromagnetic emissions
 51 in the inner magnetosphere, occurring very often within several degrees around the ge-
 52 omagnetic equator and propagating in the whistler mode with extraordinary polariza-
 53 tion (Santolík, Pickett, Gurnett, Maksimovic, & Cornilleau-Wehrin, 2002). This mode
 54 of propagation implies a nearly linear polarization of the magnetic field fluctuations (Santolík
 55 et al., 2004). The equatorial noise emissions can play a significant role in controlling the
 56 distribution of energetic electrons in the radiation belts (Horne et al., 2007). EN is de-
 57 tected mostly in the frequency range from a few hertz up to about 1 kHz, and it can be
 58 commonly observed at radial distances ranging from $2 R_E$ (Earth’s radii) up to about
 59 $8 R_E$ (Ma et al., 2013; Němec, Santolík, Pickett, Hrbáčková, & Cornilleau-Wehrin, 2013;
 60 Posch et al., 2015; Hrbáčková et al., 2015). The first observation of EN dates back to
 61 the late 1960s when Russell et al. (1970) reported a new type of noise-like emissions mea-
 62 sured by the OGO 3 satellite in the vicinity of the geomagnetic equator. It was later shown
 63 by Gurnett (1976), who analyzed the time-frequency spectrograms recorded onboard the
 64 Hawkeye 1 and Imp 6 spacecraft, that the spectrum of EN emissions consists of a com-
 65 plex superposition of harmonically spaced spectral lines. Despite this characteristic fine
 66 structure, the term equatorial “noise” is kept here for continuity reasons.

67 Perraut et al. (1982) noted that the spacing of spectral lines in the fine structure
 68 of EN is closely related to the local proton gyrofrequency f_{cp} in the EN source region
 69 and hypothesized that the emissions originate from the unstable ion ring distribution,
 70 which was observed simultaneously with an EN emission by the two GEOS spacecraft.
 71 This idea was further elaborated by several other authors (Boardsen et al., 1992; Mered-
 72 ith et al., 2008; Xiao et al., 2013) and has steadily become the prevailing theory for ex-
 73 plaining the physical origin of equatorial noise. Growth rate simulations of ion Bernstein
 74 modes with Gaussian ring distributions (Horne et al., 2000; Liu et al., 2011; Ma et al.,
 75 2014; Chen, 2015) and partial shell proton distributions centered at a pitch angle of 90°
 76 (Min & Liu, 2016) show large growth peaks at multiples of the proton gyrofrequency with
 77 the upper frequency limit set by the lower hybrid frequency f_{lh} . Subsequent propaga-
 78 tion in the whistler mode is then assumed.

79 The conversion from ion Bernstein modes with wave vectors nearly perpendicular
80 to the local magnetic field lines has implications for the wave propagation characteris-
81 tics of the EN. Perpendicular whistler mode waves starting in the equatorial region prop-
82 agate both azimuthally and radially (Kasahara et al., 1994; Santolík, Pickett, Gurnett,
83 Maksimovic, & Cornilleau-Wehrin, 2002). During inward radial motion they may reach
84 low altitudes, as was shown in the case study by Santolík et al. (2016) and statistical anal-
85 ysis of storm time EN events by Němec et al. (2016), both of which are based on DEME-
86 TER spacecraft measurements. The low frequency part of the emissions cannot prop-
87 agate further down to the Earth’s surface due to a cutoff in their mode structure, which
88 is situated between f_{cp} and the O^+ ion gyrofrequency f_{cO} . During the propagation through
89 the plasmasphere, the wave vectors remain nearly perpendicular to the ambient Earth’s
90 magnetic field (Boardsen et al., 2016), yet they are not restricted to any particular az-
91 imuthal direction (Němec, Santolík, Pickett, Hrbáčková, & Cornilleau-Wehrin, 2013).
92 It has been suggested by Santolík et al. (2016) that only those emissions that are con-
93 fined close to the meridional plane can propagate down to the altitudes of DEMETER.

94 In this article, we present statistics of low altitude EN events found in the burst
95 mode data gathered by the DEMETER spacecraft. We focus on the wave propagation
96 properties and latitudinal and frequency distributions of these emissions. The observa-
97 tional results and the methods used to obtain them are presented in Section 2. The ob-
98 served properties of EN are compared to statistics obtained from ray tracing simulations
99 in a cold plasma, which is the main topic of Section 3. We assume purely meridional prop-
100 agation (Section 3.2) and use minimization methods to estimate the distribution of wave
101 normal angles and frequencies in the source that produces the best nonlinear least-squares
102 fit of the latitudinal distribution of incident rays to the experimental data. Deviations
103 of wave vectors from the meridional plane and the expected effect of azimuthal propa-
104 gation on EN properties is analyzed separately in Section 3.3. In Sections 4 and 5 we
105 discuss the impact of the thresholds applied in data processing, the choice of our sim-
106 ulation setup and the significance of our results, and we conclude with suggestions for
107 the direction of future research.

2 Satellite Observation

2.1 Dataset and Processing Methods

The data used in the wave analysis were acquired by the ICE (system of four electrical sensors) and IMSC (triaxial set of magnetic sensors) instruments onboard the DEMETER spacecraft – see Berthelier et al. (2006) and Parrot et al. (2006) for a detailed description of these instruments. The spacecraft was operational from June 2004 to December 2010. It followed a nearly sun-synchronous circular orbit, altering between approximately 10:30 MLT and 22:30 MLT, and kept an altitude of about 710 km, later (December 2005) changed to 660 km. In the survey mode, DEMETER provided continuous wave measurements with one electric and one magnetic field component in a frequency range up to 20 kHz. More detailed data were available in the burst mode, which was triggered only in preselected regions, mostly at lower geomagnetic latitudes (Němec et al. (2007), Figure 1). Moreover, the burst mode provided waveforms of all six electromagnetic components measured with a sampling frequency of 2500 Hz, corresponding to a Nyquist frequency of 1250 Hz. With these waveforms, we can perform a detailed analysis of wave polarization and propagation properties using the singular value decomposition (SVD) methods described by Santolík et al. (2006).

In the burst mode data gathered over the 6.5 years of DEMETER operations, we found 46 EN emission events, 29 of them on the dayside and 17 on the nightside. These events were picked manually by identifying the line structure in the electric and magnetic spectra. The processed spectra of an example dayside event recorded on 2004-11-09 between 08:19:15 and 08:21:15 UT are presented in Figure 1, similar to the case analyzed by Santolík et al. (2016). In the electric and magnetic power spectrograms in Figures 1a and 1b, intense line emissions are discernible. Visual inspection of these lines shows that the spacing is approximately 20 Hz to 25 Hz, which corresponds to proton gyrofrequencies found at equatorial distances between 2.6 and 2.8 R_E if the dipole model of the geomagnetic field is assumed. This is the estimated location of the source region for this event. High values of wave magnetic field planarity parameter (Figure 1c), which measures the validity of the plane wave assumption made in the SVD analysis (Santolík et al., 2003), confirm that we are dealing with plane waves with low intensity noise in the background.

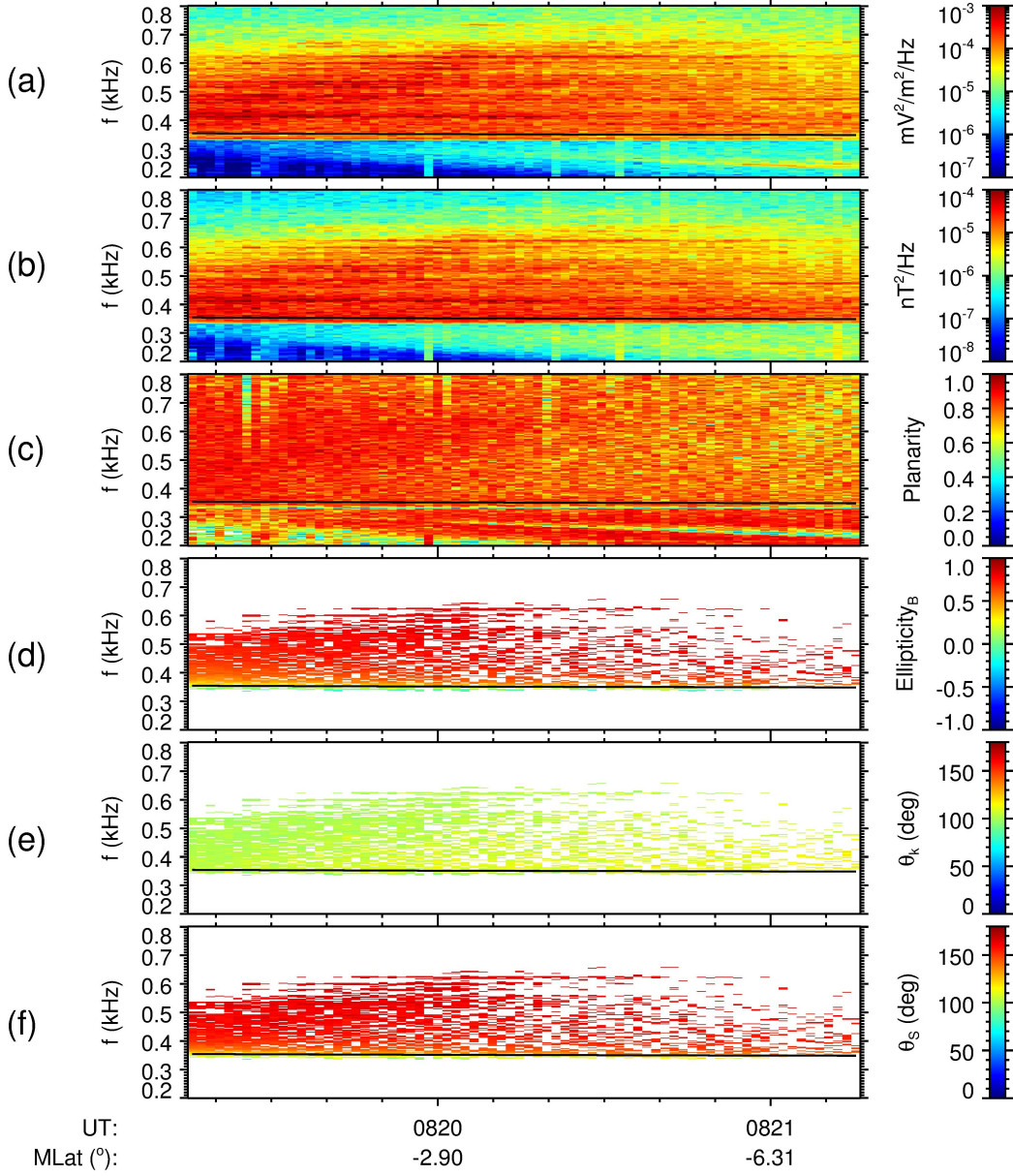


Figure 1. Time-frequency spectrograms showing wave properties of an equatorial noise event of 2004-11-09, 08:19:15 – 08:21:15 UT. a) Magnetic field PSD (Power Spectral Density), b) electric field PSD, c) planarity of polarization of the wave magnetic field, d) the ellipticity of polarization ellipse of the wave magnetic field, e) polar wave normal angle, f) polar angle of the Poynting vector. In panels d-f), magnetic field PSD and planarity thresholds are used to filter the data. The black line printed in all panels represents the local proton gyrofrequency.

139 In the analysis of wave propagation properties, we applied a threshold on the elec-
 140 tric and magnetic power-spectral densities to remove other, weaker emissions. The val-
 141 ues of the thresholds were selected manually for each event; in the example event, the
 142 values were $10^{-5} \text{ mV}^2\text{m}^{-2}\text{Hz}^{-1}$ and $10^{-5} \text{ nT}^2\text{Hz}^{-1}$. On top of that, a threshold of 0.8
 143 on the values of planarity was applied in each of the observations. In Figures 1d–1f spec-
 144 trograms of the three following wave properties are presented: ellipticity E_B (ratio of mi-
 145 nor to major axis of the polarization ellipse of the wave magnetic field with the sign added
 146 based on the sense of polarization according to Santolík, Pickett, Gurnett, and Storey
 147 (2002)), wave normal angle θ_k (Santolík et al., 2003) and the polar angle of the Poynt-
 148 ing vector θ_S (Santolík et al., 2010). We observe similar features in the spectrograms of
 149 θ_S and ellipticity, namely that both quantities attain their approximate maximum val-
 150 ues of 180° (antiparallel propagation) and 1.0 (right-hand circular polarization) every-
 151 where but in the region close to the local proton gyrofrequency f_{cp} . Here the Poynting
 152 vector becomes perpendicular to the magnetic field, and the polarization changes from
 153 right-hand circular to almost linear. The value of the wave normal angle is about 100°
 154 close to the equator for all frequencies and slightly increases its value as the spacecraft
 155 moves toward the southern hemisphere.

156 In the following statistical analysis, all data with wave frequencies below f_{cp} were
 157 excluded. This filter was added because the dispersion and polarization properties of the
 158 oblique whistler mode change rapidly below this characteristic frequency (Santolík et al.,
 159 2016), which would complicate further investigation of the results. Also, the dipole geo-
 160 magnetic latitude λ_m was replaced by λ_{Bmin} , the geomagnetic latitude centered to the
 161 geomagnetic equator, which is defined by the minimum of the Earth’s magnetic field along
 162 a field line. The minimum was obtained from the International Geomagnetic Reference
 163 Field (IGRF) and T89 magnetic field models (Tsyganenko, 1989).

164 2.2 Statistical Results

165 From all 46 equatorial noise events detected on DEMETER we constructed the dis-
 166 tributions of θ_k , θ_S and E_B in geomagnetic latitudes, which we show in Figures 2a-c. In
 167 these plots, each dot represents one time-frequency bin of the associated spectrogram,
 168 and the individual events are differentiated by color. The EN statistic shows that be-
 169 yond 22° of latitude, no equatorial noise emissions were observed. In the region within
 170 a few degrees of latitude from the equator, the waves propagate perpendicularly ($\theta_k \approx$

171 90°) with low positive values of ellipticity, implying highly elliptical right-hand polar-
 172 ization. With increasing latitude, the wave normal angle deviates from the perpendic-
 173 ular direction with an almost linear trend. This is supported by the linear least squares
 174 fit in Figure 2a with a slope of -1.08 ($R^2 = 0.71$), which goes through 90° at the equa-
 175 tor and reaches about 110° and 70° at $\lambda_{B\min} = -20^\circ$ and $\lambda_{B\min} = 20^\circ$, respectively.
 176 Ellipticity reflects this trend, becoming increasingly more circular further from the equa-
 177 tor. The polar angle of the Poynting vector is centered around 90° at low latitudes but
 178 exhibits large variance. At higher latitudes, the Poynting vector becomes nearly paral-
 179 lel in the northern hemisphere and nearly antiparallel in the southern hemisphere, which
 180 means that when the waves crossed the altitude of DEMETER, they were propagating
 181 along the field lines and away from the equator.

182 The occurrence rate of EN events is plotted in Figure 2d as a function of the mag-
 183 netic latitude. To obtain the occurrence rate, we considered each event as a box func-
 184 tion equal to one inside the latitudinal interval where it was observed and zero every-
 185 where else. These functions were then summed and normalized by the burst mode cov-
 186 erage (total number of half-orbits). All but one event are confined to the latitudinal in-
 187 terval $-20^\circ < \lambda_m < 20^\circ$ and 75% of the normalized occurrence falls within ± 9 de-
 188 grees of latitude from the magnetic equator. Figure 2e presents a histogram of the fre-
 189 quency extent of EN events; here, the events are again treated as box functions. For com-
 190 parison, we overplotted in blue the same distribution with each measurement normal-
 191 ized to f_{cp} . The axes are scaled such that $1.0f/f_{cp}$ corresponds to wave frequency $f =$
 192 321 Hz, which is the average proton gyrofrequency over all EN events. The histogram
 193 in Figure 2f reveals that most of the events were recorded during times of enhanced ge-
 194 omagnetic activity. The geomagnetic activity is quantified by the 3-hour Kp index, which
 195 ranges from 2 to 8+ with an average value of 5. However, since high Kp indices are much
 196 less probable than the low ones (see the blue line in Figure 2f), we can deduce that the
 197 probability of occurrence of low altitudinal EN events increases rapidly with increasing
 198 Kp. The connection between enhanced geomagnetic activity and EN emissions propa-
 199 gating to low altitudes was previously noticed by Němec et al. (2016) and Santolík et
 200 al. (2016).

201 Based on the presented wave analysis, we picture the propagation of EN emissions
 202 as follows: During periods of enhanced geomagnetic activity, ion Bernstein modes are
 203 generated in the magnetosphere around the plasmopause region (Němec, Santolík, Pick-

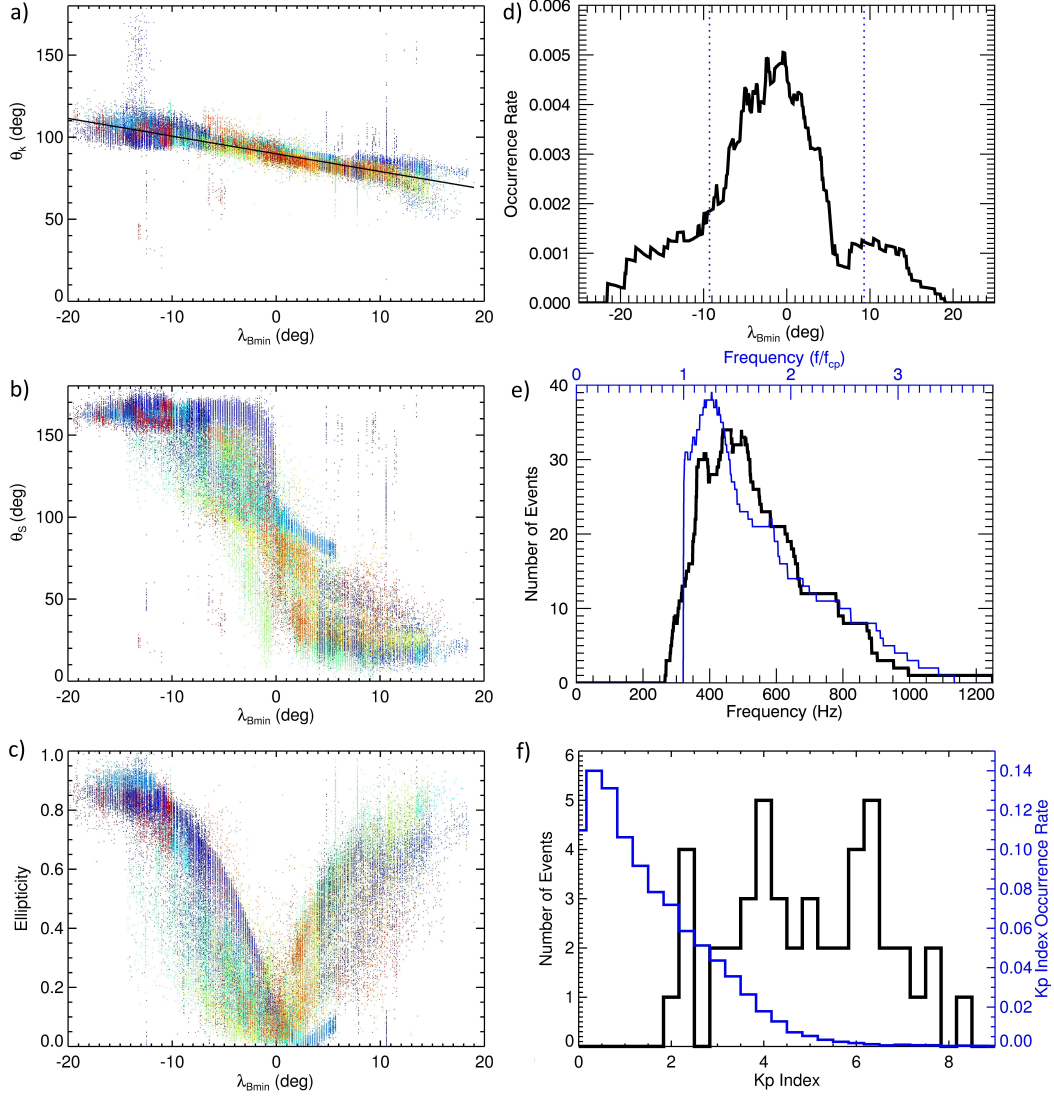


Figure 2. a) Wave normal angle. Each point represents one time-frequency bin in the corresponding spectrogram, each color represents one event. Black line shows the least square fit with the resulting linear term coefficient of -1.08 . c) Polar angle of the Poynting vector, same plot format. b) Ellipticity of the magnetic field, same plot format. d) Latitudinal distribution of events normalized to the total number of DEMETER half-orbits with burst coverage. Blue dotted lines give the symmetric interval in which falls 75% of the events. e) In black: Histogram of frequency distribution in hertz. In blue: Histogram of frequency distribution normalized to local proton gyrofrequency. Value of 1 on the upper axis corresponds to the average f_{cp} of 321 Hz on the bottom axis. f) In black: Histogram of geomagnetic activity distribution indicated by the Kp index. In blue: Occurrence rate of the values of Kp index during the whole operational period of the DEMETER spacecraft.

204 ett, Parrot, & Cornilleau-Wehrin, 2013) and subsequently converted to the whistler wave
 205 mode. Due to their nearly perpendicular wave vectors, these modes propagate down to
 206 Earth through a region confined within a narrow range of latitudes (Boardsen et al., 1992;
 207 Hrbáčková et al., 2015). At low altitudes, the emissions cross the orbit of DEMETER.
 208 When the oscillations of the wave rays within the meridional plane are negligible, we ob-
 209 serve perpendicular Poynting vectors close to the equator (see Figure 2b). Otherwise,
 210 we detect mainly quasiparallel Poynting vectors within a broader range of latitudes, with
 211 wave vectors appropriately tilted away from the perpendicular direction at higher lat-
 212 itudes. Waves with wave vectors deviating from the meridional plane are mostly deflected.
 213 The support for this EN propagation hypothesis is provided in the next sections through
 214 ray tracing simulations.

215 **3 Ray Tracing Simulation**

216 **3.1 Methods and Models**

217 To simulate the propagation of whistler-mode waves in a multicomponent cold plasma,
 218 we numerically solve 3D ray tracing equations with the 4th/5th order Dormand–Prince
 219 Runge–Kutta method from the SciPy Python library. The overall implementation is sim-
 220 ilar to the one found in Santolík et al. (2009), Section 2.3; the code and a quick guide
 221 can be downloaded from the link provided in the Open Research statement. We assume
 222 that the traversal of the plasmopause happens very early during the wave propagation
 223 so that the plasmopause can be excluded from our ray simulations. The model of elec-
 224 tron density in the Earth’s plasmasphere is adopted from Ozhogin et al. (2012), Equa-
 225 tion 2. Only electrons and protons are included in this model. At radial distances be-
 226 tween $1.3 R_E$ and $1.5 R_E$, Ozhogin’s model is smoothly connected to the diffusive equi-
 227 librium (DE) model, which is shortly summarized in Bortnik et al. (2011), Equation 2
 228 (for the original description of the diffusive equilibrium density model for the Earth’s mag-
 229 netosphere, see Angerami and Thomas (1964)). The two models are connected by cu-
 230 bic splines stretched along field lines. The values of DE model parameters, specified at
 231 the reference radial distance $h_0 = 660$ km (the altitude of DEMETER), were chosen
 232 as follows: electron density $n_{e0} = 3 \cdot 10^4 \text{ cm}^{-3}$, ion temperature $T_{i0} = 850$ K and rela-
 233 tive ion densities $\delta n_{p0} = 0.25$ and $\delta n_{O+0} = 0.75$. According to the IRI model (Bilitza,
 234 2018), these values are quite typical for dayside ionosphere at the equator during mod-
 235 erate or low solar activity. Any longitudinal variance in absolute or relative densities is

236 assumed to be negligible. The Earth’s magnetic field is modeled by a perfect dipole, with
 237 the equatorial magnetic field strength at the surface set to $3.03 \cdot 10^{-5}$ T. The dipole ge-
 238 omagnetic latitude λ_m and the geomagnetic latitude centered to the minimum of the ge-
 239 omagnetic field $\lambda_{B_{\min}}$ naturally coincide in this model.

240 While the ray tracing code is fully 3D and thus allows for azimuthal propagation,
 241 the next section focuses on purely meridional propagation, i.e., the initial azimuthal an-
 242 gles of the wave vector ϕ_{k0} is set to 180° . As we already mentioned in the introduction,
 243 it is unlikely that emissions propagating away from the initial meridional plane will reach
 244 the altitudes of DEMETER (Santolík et al., 2016). Nevertheless, to support this claim
 245 about preferential radial propagation, the effects of deviation of ϕ_{k0} from 180° are an-
 246 alyzed in Section 3.3.

247 **3.2 Meridional Propagation**

248 **3.2.1 Simulation Setup**

249 The initial values of ray parameters are based on our knowledge of the generation
 250 mechanism of EN and on the frequency histogram shown in Figure 2e. Source location
 251 at exactly $\lambda_m = 0^\circ$ is assumed, with radial distances ranging from $2.2 R_E$ to $3.2 R_E$ with
 252 a step of $0.05 R_E$. According to O’Brien and Moldwin (2003), the average plasmopause
 253 distance L_{pp} corresponds to the chosen source location for Kp indices from 6+ to 9–,
 254 but it should be noted that the $L_{pp}(\text{Kp})$ dependence displays a large variance. In ad-
 255 dition, the simulated rays are assumed to start at the inner edge of the plasmopause and
 256 not at its center, thus further justifying the low values of initial radial distance.

257 With our magnetic field and density models, we can determine the range of equa-
 258 torial lower hybrid frequencies $f_{lh} = 580$ Hz (largest initial distance) to $f_{lh} = 1740$ Hz
 259 (smallest initial distance). The L -cutoff of the whistler dispersion branch (Stix, 1992)
 260 calculated at the altitudes of DEMETER is approximately $f_{L=0} = 260$ Hz. We also know
 261 from our observations that there are no emissions observed above approximately 1200 Hz.
 262 With all these considerations in mind, we set the range of wave frequencies to 240 Hz –
 263 1200 Hz spaced by 20 Hz, supplemented with the condition $f < f_{lh}$.

264 The initial wave normal angles are chosen from the range $\theta_{k0} = 85^\circ$ to $\theta_{k0} = 90^\circ$
 265 with a step of 0.1° . Due to the unknown hot proton distributions in the source region,

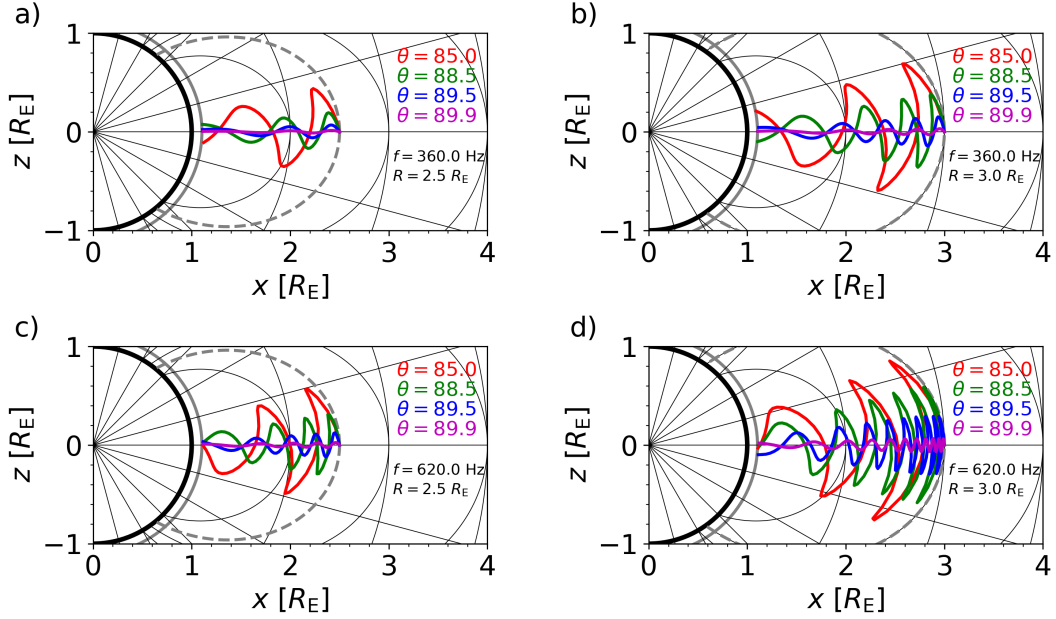


Figure 3. Propagation of selected rays with initial azimuthal angle $\phi_{k0} = 180^\circ$. The grey dashed line represents the initial L -shell of traced rays, the solid grey arc marks the orbital altitude of DEMETER. Thin black lines represent radial distances (with a step of $1 R_E$), latitudes (with a step of 15°) and L -shells (integer values). Individual ray trajectories are color-coded by their initial wave normal angle. Wave frequency and initial radial distance are given in each panel.

266 we cannot calculate the appropriate range of θ_{k0} , but based on linear growth calculations
 267 we can assume that the distribution should not be uniform but rather peaked around
 268 90° (Chen, 2015; Min & Liu, 2016) – this issue will be addressed later in Section 3.2.3.

269 **3.2.2 Ray Propagation Examples**

270 The combination of input parameters and frequency limitations amounts to 49662
 271 traced rays. As expected, all the rays with frequencies lower than the cutoff frequency
 272 $f_{L=0}$ at the altitudes of DEMETER were reflected, as well as most rays with frequen-
 273 cies 260 Hz and 280 Hz, which are still too close to the cutoff. At these low frequencies,
 274 the WKB (Wentzel-Kramers-Brillouin) condition was sometimes violated during the re-
 275 flection, especially in cases with very low values of $|\theta_{k0} - 90^\circ|$, reminding us of the lim-
 276 itations of the ray approximation.

277 In Figure 3 we show the resulting ray trajectories for some representative values
 278 of initial parameters. The initial L -shell and terminal altitude are marked by a dashed
 279 grey line and a solid grey line, respectively, and the coordinates λ_m , R and L are indi-
 280 cated by thin black lines. As the rays propagate down to Earth, their trajectories oscil-
 281 late in latitude, where the amplitude of oscillations grows with the initial deviation of
 282 the wave normal angle, the initial distance, and the wave frequency. Higher frequency
 283 also leads to an increased number of equator crossings. Larger oscillation amplitudes may
 284 result in larger absolute values of final latitudes, but as shown in panel d), even wildly
 285 oscillating trajectories (red line, $\theta_{k0} = 85^\circ$) can arrive at the altitudes of DEMETER
 286 while crossing the magnetic equator. The latitudinal extent of the oscillations remains
 287 almost constant during the propagation.

288 **3.2.3 Comparison with the Observations**

289 For comparison of ray tracing results with experimental observations, we removed
 290 all rays with final f/f_{cp} ratio below 1, leaving us with 43028 rays in total (note that this
 291 condition leaves out the case studied by Santolík et al. (2016)). Furthermore, the sym-
 292 metric trajectories with initial wave normal angles $90^\circ - \theta_{k0}$ are added, increasing the
 293 number of rays to 86056. 98.9% of those reach the altitude of DEMETER. The simu-
 294 lated wave propagation properties are presented in Figure 4 as histograms of the inci-
 295 dent ray count. The bin sizes are as follows: 0.5° in λ_m , 1° in θ_k and θ_S , and 0.05 in E_B .
 296 The latitudes are limited to the interval from -30° to 30° , into which falls 98.5% of the
 297 rays that reached the terminal altitude.

298 Looking at the general trends, we can see that the wave normal angles (Figure 4a)
 299 increasingly deviate from 90° as the rays fall farther from the equator, and that the growth
 300 of the deviation has a mostly linear dependence on latitude. However, we notice that the
 301 spread of θ_k is considerably larger than in the experimental data. We quantify the trend
 302 by a linear fit (green dashed line), which now has a slope of -1.81 , a much larger value
 303 compared to the slope of -1.08 calculated for the DEMETER data. The simulated Poynt-
 304 ing vector angle θ_S also has the same general behavior as in the observational data, but
 305 most of the data points are concentrated near the parallel and antiparallel direction (more
 306 precisely, near 160° and 20°), with only 17% of rays falling into the range from 45° to
 307 135° . Similarly, the magnetic field ellipticity obtained through SVD methods (Santolík
 308 et al., 2003) also follows the trend set by the DEMETER data, but with a higher pref-

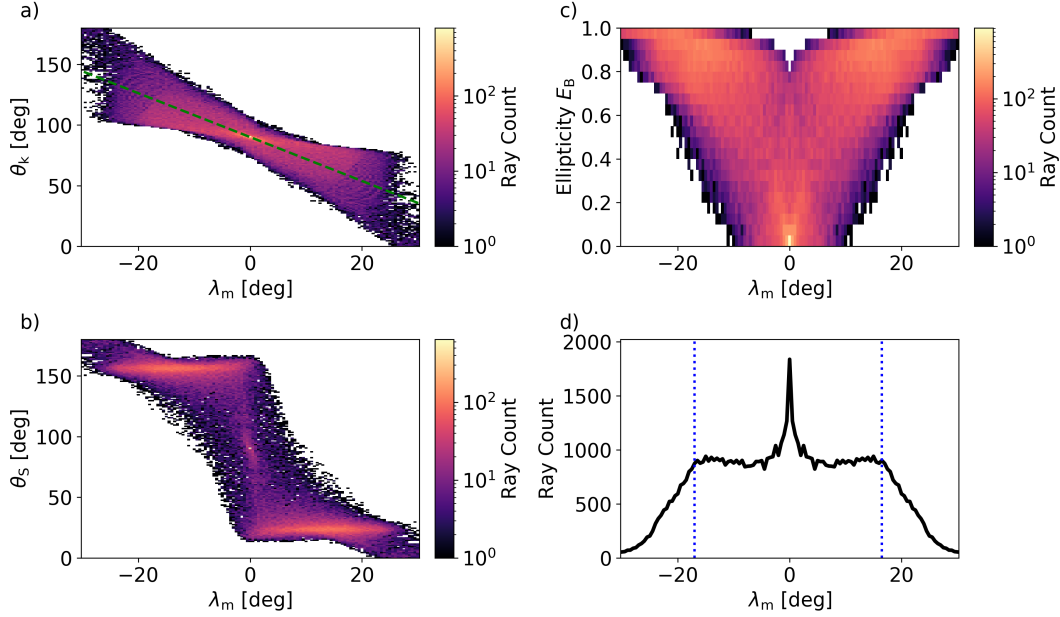


Figure 4. The same wave properties and distributions as in Figures 2a-d, plotted as histograms of the number of simulated rays reaching low altitudes. The green dashed line in panel a) is the linear least squares fit through all data points, with a slope of -1.81 . In panel d) blue dotted lines give the $\pm 17^\circ$ symmetric interval in which falls 75 % of the rays.

309 erence towards values above 0.5. The increase in E_B values happens at very low altitudes,
 310 while the distribution of ellipticity in the source region always remains concentrated near
 311 zero, in agreement with spacecraft observations (Santolík et al., 2004).

312 Overall, we showed a good qualitative agreement between the experiment and the
 313 simulation, confirming that the unusual properties of low altitude equatorial noise re-
 314 sult from the propagation pattern of near-perpendicular whistler mode waves in the cold
 315 plasma of the plasmasphere. Nevertheless, there are noticeable discrepancies, which are
 316 probably best highlighted in panel d) of Figure 4, where we plot the distribution of in-
 317 cident rays across latitude. Apart from the sharp peak located right at the equator, the
 318 distribution is nearly uniform up to about $\lambda_m = 18^\circ$, where it starts falling off. The
 319 blue dotted lines at $\pm 17^\circ$ delimit the interval into which falls 75 % of rays, which is a
 320 marked increase from the $\pm 9^\circ$ interval obtained with the DEMETER data. This increased
 321 spread in latitudes suggests that either the models we are using are not suitable or that
 322 the input values of the wave properties do not match the properties of the source of the
 323 equatorial noise.

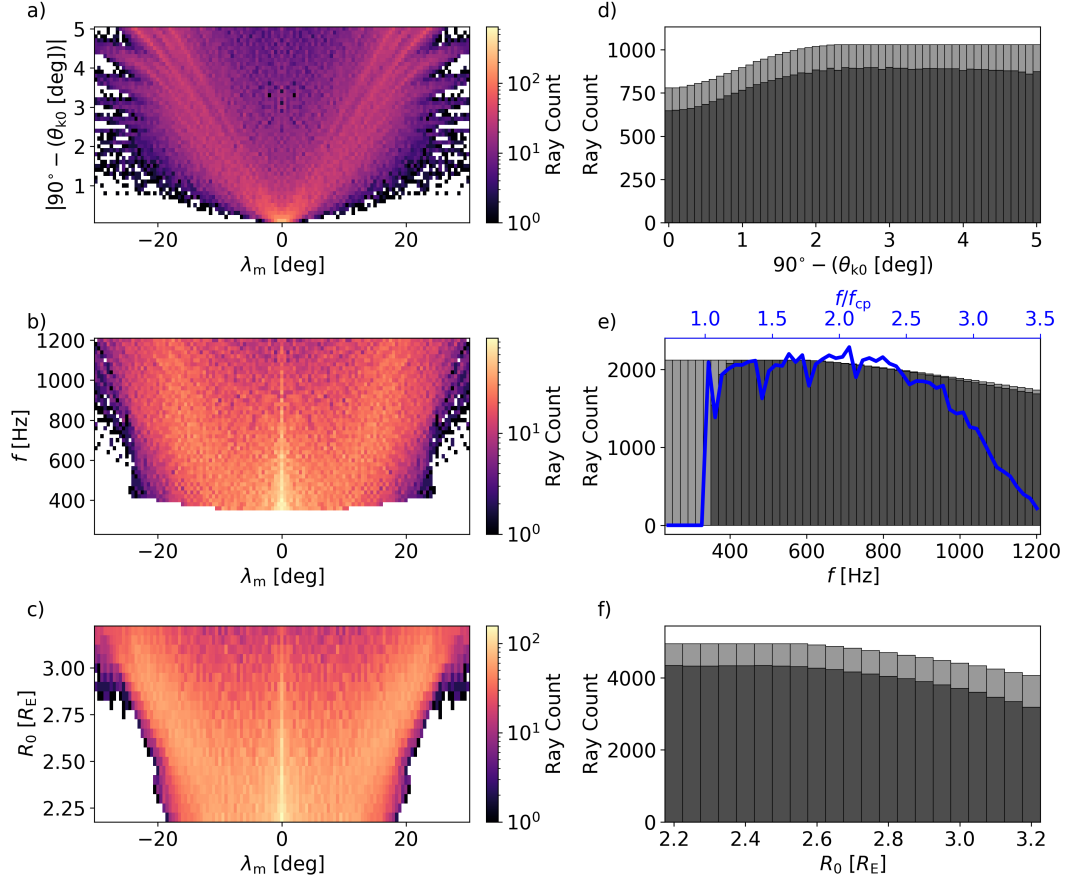


Figure 5. a-c) 2D histograms of incident rays in space of magnetic latitude and (a) initial wave normal angle θ_{k0} , (b) wave frequency f , and (c) polar angle of the Poynting vector θ_S . d-c) 1D histograms of the input parameters plotted in panels a-c). Light grey bars correspond to all initiated rays, dark grey bars represent only those rays which reached the altitude of DEMETER and had $f/f_{cp} > 1$ at the terminal point.

324 Leaving the question of the adequacy of magnetic field and density models for the
 325 discussion in Section 4, we now focus on modifying the set of input parameters. Figures
 326 5a-c show similar histograms as Figures 4a-c, but the wave properties at low altitude are
 327 now replaced by the initial wave normal angle θ_{k0} (bin size 0.1°), wave frequency f (bin
 328 size 20 Hz) and initial radial distance (bin size $0.05 R_E$). We make several observations
 329 based on these histograms. Firstly, all rays with θ_{k0} deviating less than $\pm 0.7^\circ$ from the
 330 perpendicular direction land within $\pm 20^\circ$ of the equator. Therefore, we must limit the
 331 initial spread in wave normal angles to improve the agreement between simulated and
 332 observed latitudinal distribution. Secondly, rays with large initial deviations follow a bi-
 333 modal distribution in latitudes, with only a small amount arriving near the equator. Rays
 334 with higher frequencies and larger initial distances also contribute predominantly to higher
 335 latitudes, but the dependence is less pronounced than in the case of θ_{k0} .

336 Figures 5d-f show the 1D histograms of the input ray parameters. Light grey his-
 337 tograms show the number of all rays that were started (not symmetrized in panel d), and
 338 the dark grey bars show the rays which arrived at the altitudes of DEMETER and sat-
 339 isfied the condition $f/f_{cp} > 1$. We notice that due to the lower hybrid resonance im-
 340 posing an upper limit on the whistler mode frequencies, the number of rays decreases
 341 with θ_{k0} approaching 90° , which is exactly the opposite of what we would expect from
 342 a realistic source of EN. The histogram of frequencies shows a decreasing trend start-
 343 ing at 440 Hz, but the drop off is much slower than in the observed frequency distribu-
 344 tion (Figure 2e) and is almost exclusively due to the lower hybrid resonance. Lastly, we
 345 show the histogram of initial radial distances, which also exhibits a downward trend as-
 346 sociated with f_{lh} .

347 We now introduce a gaussian weighting function

$$w(\theta_{k0}; \sigma_\theta) = \exp\left(\frac{-(\theta_{k0} - 90^\circ)^2}{2\sigma_\theta^2}\right) \quad (1)$$

348 to model the distribution of the initial wave normal angles. The initial frequency dis-
 349 tribution is divided into 4 bins with edge values [240, 480, 720, 960, 1200] Hz, and to each
 350 bin we assign a normalization factor a_i , $i \in \{1, 2, 3, 4\}$. The distribution of initial dis-
 351 tances is not weighted but is indirectly influenced by the distribution of θ_{k0} and f through
 352 the cold plasma dispersion relation of the whistler mode. In total, we have 5 param-
 353 eters (σ_θ , a_1 , a_2 , a_3 , a_4) which are determined by the nonlinear least squares fit of the

354 histogram of the latitude of incident rays to the occurrence plot in Figure 2d. For the
 355 purpose of the fitting procedure, the experimental data are rebinned to λ_{Bmin} bins of 0.5° .

356 The optimal parameters were found with the Levenberg–Marquardt algorithm (as
 357 implemented in SciPy, Moré (1978)). Because it does not ensure that global minima will
 358 be found, we tried five different guesses of σ_θ , increasing from 1° to 5° with a step of 1° .
 359 The frequency distribution normalization factors were set to $a_1 = 1.0$, $a_2 = 1.0$, $a_3 =$
 360 0.25 and $a_4 = 0.0625$, approximately following the distribution obtained from the DEME-
 361 TER data. The resulting best fit parameters are: $\sigma_\theta = 2.01^\circ$, $a_1 = 0.59$, $a_2 = 0.37$,
 362 $a_3 = 0.0$ and $a_4 = 0.040$ (sum of a_i has been normalized to 1). The histograms from
 363 Figure 4 are recalculated with the obtained weights and presented in Figure 6. The quan-
 364 titative agreement between simulation and experiment has clearly improved, as shown
 365 by the decrease in the slope of the linear fit of θ_k data from -1.81 to -1.60 , and by the
 366 narrowing of the occurrence histogram in latitudes. 75 % of the rays now fall within $\pm 10^\circ$
 367 around the equator, which almost matches the experimental value of $\pm 9^\circ$. Extreme val-
 368 ues of all three wave propagation parameters θ_k , θ_S and E_B are now overall less pronounced.

369 An alternative option of keeping a_i fixed and fitting only the standard deviation
 370 of θ_{k0} distribution results in $\sigma_\theta = 1.42^\circ$ and the linear fit of $\theta_k(\lambda_m)$ then has a slope
 371 of -1.50 . However, the simulated frequency histogram then does not match the exper-
 372 imental results and the sum of squares of residuals increases. Ideally, we should try to
 373 minimize the residuals not only for the experimental distribution of latitudes in Figure
 374 2d, but across all experimental histograms in Figures 2a-e; unfortunately, there is no re-
 375 liable method that would prescribe a weight or importance to each histogram.

376 **3.3 Azimuthal Propagation**

377 **3.3.1 Simulation Setup**

378 Apart from the meridional propagation of the large set of rays, we also present the
 379 3D tracing of another, smaller set of rays with azimuthal angles ranging from 170.0° to
 380 179.8° (step 0.2°). The other wave parameters are restricted followingly: θ_k goes from
 381 88.50° to 89.95° (step 0.05°), frequencies are set to 360 Hz and 620 Hz and radial dis-
 382 tances to $2.5 R_E$ and $3.0 R_E$. In total, 6000 rays were traced. The questions we aim to
 383 resolve with this simulation are these: for which values of the initial azimuthal angle ϕ_{k0}

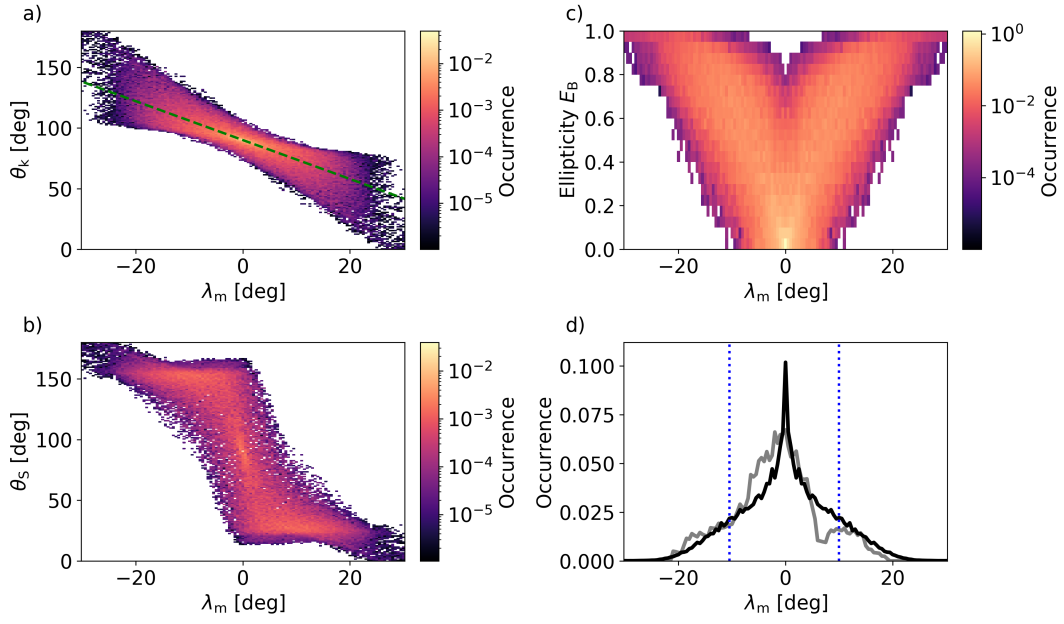


Figure 6. Histograms of the number of incident rays. Same types of plots as in Figure 4, but with weighting functions imposed in the initial ray tracing parameters according to a nonlinear least squares method (see text). Linear fit through the wave normal angles against latitudes in panel a) has a slope of -1.60 . In panel d), the experimental occurrence of low altitude noise is overlaid in grey, and the 75% symmetric interval is shown by vertical blue dotted lines.

384 can the rays reach DEMETER, and how do the final values of λ_m , θ_k and longitude de-
 385 pend on the choice of ϕ_{k0} .

386 **3.3.2 Ray Propagation Statistics**

387 In Figure 7 we show 2D plots of terminal wave normal angles, latitudes and lon-
 388 gitudes in (θ_{k0}, ϕ_{k0}) space. First, let us look at the behavior of the plots for $\phi_{k0} > 179^\circ$.
 389 As the deviation of θ_{k0} from 90° increases, the latitudes and wave normal angles at the
 390 altitudes of DEMETER start to oscillate. The oscillations become faster and more pro-
 391 nounced as the distance and frequency increase; this is similar to the observations made
 392 on ray trajectories plotted in Figure 3. The terminal longitude is nearly independent of
 393 the initial wave normal angle, and its value remains near 0° (in the same magnetic merid-
 394 ian as the source), with only a slight increase with frequency and initial distance.

395 As we move to $\phi_{k0} < 179^\circ$, the behavior changes. The oscillations in the latitudes
 396 and wave normal angles slightly increase in amplitude, and the rays can reach longitudes
 397 of up to about 50° from the source magnetic meridian. At a certain point, due to the
 398 azimuthal component of the wave vector increasing, the rays experience reflection be-
 399 fore reaching the desired altitude. The minimum ϕ_{k0} which enables crossing of the ray
 400 trajectory with the altitude of DEMETER is approximately 174° for $f = 360$ Hz and
 401 $R_0 = 2.5 R_E$ and shows almost no dependence on θ_{k0} . On the other hand, rays started
 402 at $R_0 = 3.0 R_E$ with frequency $f = 620$ Hz are limited to $\phi_{k0} > 178^\circ$ for $\theta_{k0} = 89.95^\circ$,
 403 and the interval of ϕ_{k0} increases with the deviation of the initial wave normal angle from
 404 90° up to $\phi_{k0} > 177^\circ$ for $\theta_{k0} = 88.50^\circ$. We have thus proven that the equatorial noise
 405 can reach DEMETER only when the initial deviation from the radial direction in azimuth
 406 is only a few degrees or less, and the limit decreases rapidly with wave frequency and
 407 initial distance. Moreover, the MLT of the observation can reach over 2 hours from the
 408 source location only with ϕ_{k0} very close to the deflection threshold. These findings jus-
 409 tify our approach from Section 2 where the experimental data were compared to results
 410 obtained from ray propagation restricted to the meridional plane.

411 Our findings on longitudinal propagation and ray deflection can be compared with
 412 an analytic estimate of the lowest altitude reached by the rays based on the conserva-
 413 tion of the geometric invariant

$$Q = \mu R \sin \phi_S. \quad (2)$$

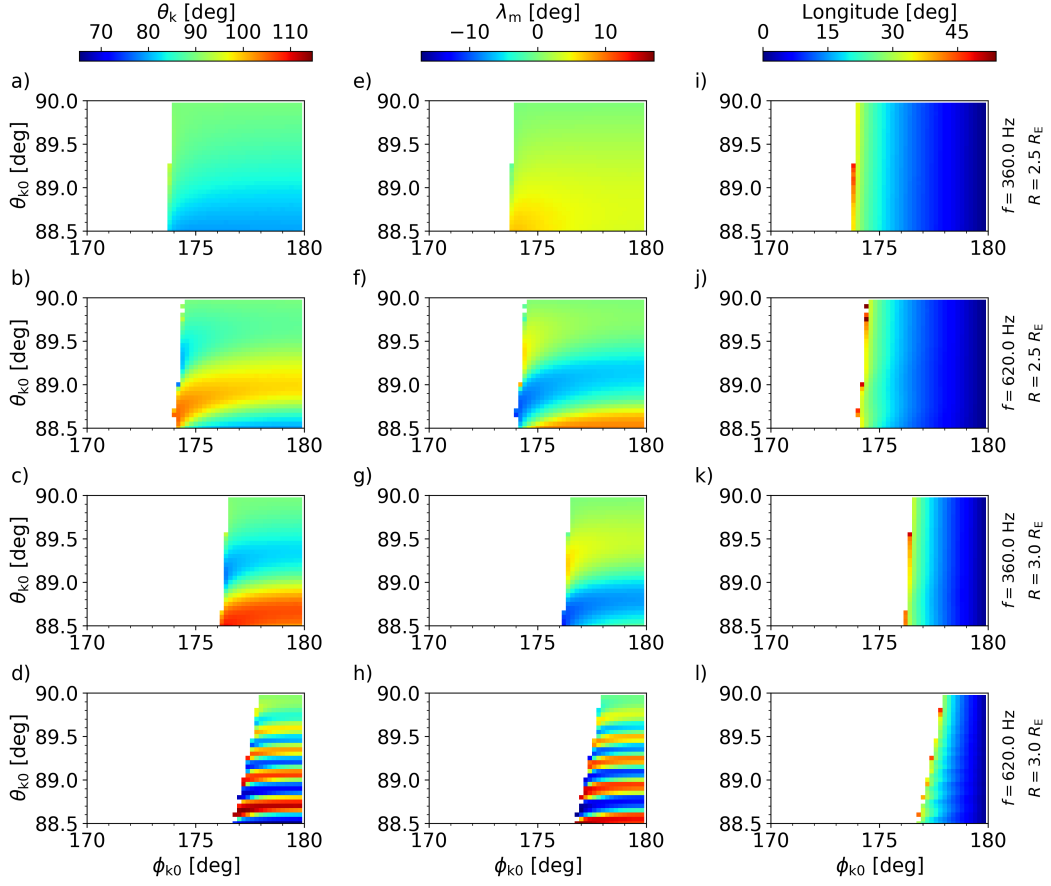


Figure 7. a-d) Wave normal angles of simulated rays after reaching the altitude of DEMETER, plotted as a function of the initial wave normal angle θ_{k0} and the initial azimuthal angle ϕ_{k0} . e-h) Latitude where rays crossed the altitude of DEMETER, same plot format as in a-d). i-l) Longitude where rays crossed the altitude of DEMETER, same plot format as in a-d). On the right side of the figure, initial radial distances and wave frequencies are indicated for each triplet of plots.

414 Here, μ denotes the refractive index and ϕ_S is the azimuthal deviation angle of the Poynting
 415 vector from the direction towards the Earth's surface. For Q to be truly invariant,
 416 the propagation medium must be axially symmetric, and the ray trajectories must lie
 417 in the equatorial plane (for more details, see Chen and Thorne (2012), Section 2). There-
 418 fore, we can analyze only waves with a constant $\theta_k = 90^\circ$ by this method. Notice that
 419 due to the axial symmetry of the plasma medium, the azimuthal angle of the Poynting
 420 vector and the wave vector coincide. By tracking the evolution of refractive index along
 421 the path of rays with $\theta_{k0} = 89.95^\circ$, we can confirm that the values of ϕ_{k0} at which the
 422 rays start experiencing deflection from Earth matches the theoretical prediction. Because
 423 results presented in Figure 7 show that θ_{k0} does not have much impact on the range of
 424 ϕ_{k0} for lower values of frequency and R_0 , Equation 2 can be used in these cases to de-
 425 termine which rays can reach the altitudes of low orbit spacecraft.

426 **4 Discussion**

427 In the analysis of electromagnetic data from DEMETER, we decided to remove all
 428 frequencies below the local proton gyrofrequency. That way, we completely excluded the
 429 event studied by Santolík et al. (2016) from our dataset. In this case study, the reported
 430 equatorial noise emission occurred within 10° of the equator, with θ_k very close to 90° ,
 431 and at frequencies extending below $f_{cp}/2$. Dispersion properties at these frequencies strongly
 432 depend on the ion composition, which would increase the number of parameters in our
 433 analysis. Of all the frequency-time intervals with EN in our dataset, after applying the
 434 thresholds on power density and planarity, only 27.6% fall under f_{cp} , and therefore we
 435 have chosen not to include this smaller, special part of the dataset in our analysis.

436 In the comparison of the ray tracing results with the experimental data (Section
 437 3.2.3), we encountered some difficulties related to the choice of input and output param-
 438 eters. We chose to compare the occurrence of equatorial noise in magnetic latitudes, but
 439 we could have chosen the occurrence in a two-dimensional space of latitude and a selected
 440 wave propagation property. Our decision was motivated by the fact that the total num-
 441 ber of events is relatively low, so the 2D histograms might not be representative of the
 442 whole statistical population due to the larger space that needs to be sampled.

443 There is also no rigorous way to determine the optimal size of bins in the histogram,
 444 apart from the requirement that the total number of bins (output parameters) must be

445 larger than or equal to the number of the input parameters. We decided to keep the num-
 446 ber of input parameters as low as reasonably possible, which is why the frequency dis-
 447 tribution was divided only into four bins with a corresponding number of normalization
 448 factors. Unlike in the case of the θ_{k0} distribution, we do not have a model of the frequency
 449 distribution that could be described by an elementary function. The distribution in ini-
 450 tial radial distances was not parametrized because the histogram of ray occurrence in
 451 the R_0 and λ_m space is very similar to the histogram in the f and λ_m space, and so it
 452 would be problematic to separate the influence of frequency on the occurrence in lati-
 453 tudes from the influence of the initial distance.

454 Despite the complexity of the relations between the various input and output pa-
 455 rameters of the system, we achieved a solid agreement between the weighted latitudi-
 456 nal histogram and its experimental counterpart. Unfortunately, the sharp peak near $\lambda_m =$
 457 0° could not be removed by the weighting procedure. We hypothesize that the absence
 458 of this peak in the observational data comes from the simple fact that the source of EN
 459 is not located precisely at $\lambda_{Bmin} = 0^\circ$, but has a small spread along the local field line
 460 which results in a smearing of the histogram.

461 The effects of the azimuthal component of the wave vector on the propagation of
 462 equatorial noise to low altitudes were studied previously by Santolík et al. (2016). Based
 463 on a ray tracing simulation, they concluded that the initial azimuthal angle must not
 464 deviate by more than 1° from the radial direction, and thus that only a small fraction
 465 of equatorial noise waves can propagate down to the DEMETER orbit. As we have shown
 466 in Figure 7, the available range of azimuth increases with decreasing initial radial dis-
 467 tance and frequency. As long as the distribution of θ_{k0} is very narrow, Equation 2 gives
 468 a good estimate on the range of ϕ_{k0} for a given radial distance of the source; however,
 469 the initial distance cannot be reliably estimated from the line spectrum, because in most
 470 cases, the spectrograms feature overlapping lines associated with multiple sources act-
 471 ing at different radial distances at the same time.

472 Some aspects of the propagation of equatorial noise were omitted entirely from our
 473 ray tracing analysis. First, we decided to use a single model of the ionosphere instead
 474 of dividing the simulation models into ray propagation during day and night. This choice
 475 is acceptable as long as we ignore the waves below proton gyrofrequency. Otherwise, the
 476 density ratio of oxygen to hydrogen ions would play a significant role in the computa-

477 tion of the refractive index at the low frequency part of the EN emission spectrum, and
 478 as was shown by the ion measurements from DEMETER (Gladyshev et al., 2012), or as
 479 predicted by the IRI model (Bilitza, 2018), the ion composition varies as a function of
 480 MLT. It also depends on the latitude, but this becomes important only at higher lati-
 481 tudes. And second, the ray propagation depends on the model of plasmaspheric electron
 482 density. We expect that the density gradient along field lines can influence the spread
 483 of EN occurrence in latitudes and the wave propagation properties observed on DEME-
 484 TER.

485 5 Conclusion

486 We analyzed electromagnetic wave data of low-altitudinal equatorial noise emis-
 487 sions measured during the whole mission of the DEMETER spacecraft and presented
 488 the statistics of wave propagation properties of those emissions, namely wave normal an-
 489 gle, polar angle of the Poynting vector, the ellipticity of polarization, latitudinal distri-
 490 bution and frequency distribution. The emissions are observed within about 20° of the
 491 geomagnetic equator with wave normal angles mostly between 60° and 120° , while the
 492 polar angle of the Poynting vector ranges across the whole range from 0° to 180° , with
 493 the very high and very low values being dominant farther from the equator. We have
 494 also confirmed that the occurrence of these emissions is accompanied by strong geomag-
 495 netic activity, as was indicated earlier by Němec et al. (2016).

496 Comparison of the observational data with a numerical ray tracing experiment con-
 497 firms that the observation is in good agreement with the theory of wave propagation in
 498 cold plasma under suitable assumptions about the nature of the source region. We also
 499 showed that the possible initial azimuthal angles are limited to only a few degrees around
 500 the radial downward direction, and this interval decreases with growing frequency and
 501 initial radial distance. This behavior explains why the equatorial noise can be observed
 502 at low altitudes predominantly in periods of very high geomagnetic activity, during which
 503 the source region probably moves closer to the Earth.

504 The analysis presented in this paper could be improved by acquiring simultaneous
 505 measurements of EN and hot proton distributions in the source region and consequent
 506 calculation of growth rates, providing thus solid support for the choice of initial wave prop-
 507 erties. Also, a larger experimental dataset could reveal more detailed features of the sta-

508 tistical behavior of wave propagation parameters. Furthermore, we left open the ques-
 509 tion of the effect of the electron density model on the propagation properties of the equa-
 510 torial noise emissions, and we did not address the behavior of the part of the emission
 511 reaching below the local proton gyrofrequency. These points will be investigated in fu-
 512 ture studies.

513 **Open Research**

514 DEMETER spacecraft data are accessible from <https://sipad-cdpp.cnes.fr>.
 515 The processed equatorial noise data used in this paper and related IDL procedures can
 516 be found at <https://doi.org/10.6084/m9.figshare.19208646.v1>. Kp indices can be
 517 downloaded from the World Data Center for Geomagnetism, Kyoto <http://wdc.kugi>
 518 [.kyoto-u.ac.jp/dstae/index.html](http://wdc.kugi.kyoto-u.ac.jp/dstae/index.html). The ray tracing code and associated input files
 519 and Python plotting procedures can be found at [https://doi.org/10.6084/m9.figshare](https://doi.org/10.6084/m9.figshare.19181864.v1)
 520 [.19181864.v1](https://doi.org/10.6084/m9.figshare.19181864.v1).

521 **Acknowledgments**

522 This work has received funding from the European Union’s Horizon 2020 research and
 523 innovation programme under grant agreement No. 870452 (PAGER). The work of MH
 524 and OS was supported from the GA UK project No. 64120. The work of FN was sup-
 525 ported from the GACR project No. 21-01813S. We thank the engineers from CNES and
 526 scientific laboratories (CBK, IRAP, LPC2E, LPP, and SSD of ESTEC) who largely con-
 527 tributed to the success of the DEMETER spacecraft mission.

528 **References**

- 529 Angerami, J. J., & Thomas, J. O. (1964, November). Studies of Planetary Atmo-
 530 spheres, 1, The Distribution of Electrons and Ions in the Earth’s Exosphere. *J.*
 531 *Geophys. Res.*, *69*, 4537-4560. doi: 10.1029/JZ069i021p04537
- 532 Berthelier, J. J., Godefroy, M., Leblanc, F., Malingre, M., Menvielle, M., Lagoutte,
 533 D., ... Pfaff, R. (2006, April). ICE, the electric field experiment on DEME-
 534 TER. *Planet. Space Sci.*, *54*, 456-471. doi: 10.1016/j.pss.2005.10.016
- 535 Bilitza, D. (2018, September). IRI the International Standard for the Ionosphere.
 536 *Adv. Radio Sci.*, *16*, 1-11. doi: 10.5194/ars-16-1-2018
- 537 Boardsen, S. A., Gallagher, D. L., Gurnett, D. A., Peterson, W. K., & Green, J. L.

- (1992, October). Funnel-shaped, low-frequency equatorial waves. *J. Geophys. Res. Space Physics*, *97*, 14967-14976. doi: 10.1029/92JA00827
- Boardsen, S. A., Hospodarsky, G. B., Kletzing, C. A., Engebretson, M. J., Pfaff, R. F., Wygant, J. R., . . . De Pascuale, S. (2016, April). Survey of the frequency dependent latitudinal distribution of the fast magnetosonic wave mode from Van Allen Probes Electric and Magnetic Field Instrument and Integrated Science waveform receiver plasma wave analysis. *J. Geophys. Res. Space Physics*, *121*, 2902-2921. doi: 10.1002/2015JA021844
- Bortnik, J., Chen, L., Li, W., Thorne, R. M., & Horne, R. B. (2011, August). Modeling the evolution of chorus waves into plasmaspheric hiss. *J. Geophys. Res. Space Physics*, *116*, A08221. doi: 10.1029/2011JA016499
- Chen, L. (2015, June). Wave normal angle and frequency characteristics of magnetosonic wave linear instability. *Geophys. Res. Lett.*, *42*, 4709-4715. doi: 10.1002/2015GL064237
- Chen, L., & Thorne, R. M. (2012, July). Perpendicular propagation of magnetosonic waves. *Geophys. Res. Lett.*, *39*, L14102. doi: 10.1029/2012GL052485
- Gladyshev, V. A., Shchekotov, A. Y., Yagova, N. V., Berthelier, J. J., Parrot, M., Akent'eva, O. S., . . . Molchanov, O. A. (2012, April). Concentration of ions in the topside ionosphere as measured onboard the DEMETER satellite: Morphology and dependence on solar and geomagnetic activity. *Cosmic Research*, *50*(2), 103-115. doi: 10.1134/S0010952512020037
- Gurnett, D. A. (1976, June). Plasma wave interactions with energetic ions near the magnetic equator. *J. Geophys. Res.*, *81*, 2765. doi: 10.1029/JA081i016p02765
- Horne, R. B., Thorne, R. M., Glauert, S. A., Meredith, N. P., Pokhotelov, D., & Santolík, O. (2007, September). Electron acceleration in the Van Allen radiation belts by fast magnetosonic waves. *Geophys. Res. Lett.*, *34*(17), L17107. doi: 10.1029/2007GL030267
- Horne, R. B., Wheeler, G. V., & Alleyne, H. S. C. K. (2000, December). Proton and electron heating by radially propagating fast magnetosonic waves. *J. Geophys. Res. Space Physics*, *105*, 27597-27610. doi: 10.1029/2000JA000018
- Hrbáčková, Z., Santolík, O., Němec, F., Macúšová, E., & Cornilleau-Wehrlin, N. (2015, February). Systematic analysis of occurrence of equatorial noise emissions using 10 years of data from the Cluster mission. *J. Geophys. Res. Space*

- 571 *Physics*, 120, 1007-1021. doi: 10.1002/2014JA020268
- 572 Kasahara, Y., Kenmochi, H., & Kimura, I. (1994, July). Propagation characteris-
573 tics of the ELF emissions observed by the satellite Akebono in the magnetic
574 equatorial region. *Rad. Sci.*, 29(4), 751-767. doi: 10.1029/94RS00445
- 575 Liu, K., Gary, S. P., & Winske, D. (2011, July). Excitation of magnetosonic waves
576 in the terrestrial magnetosphere: Particle-in-cell simulations. *J. Geophys. Res.*
577 *Space Physics*, 116, A07212. doi: 10.1029/2010JA016372
- 578 Ma, Q., Li, W., Chen, L., Thorne, R. M., & Angelopoulos, V. (2014, February).
579 Magnetosonic wave excitation by ion ring distributions in the Earth's in-
580 ner magnetosphere. *J. Geophys. Res. Space Physics*, 119, 844-852. doi:
581 10.1002/2013JA019591
- 582 Ma, Q., Li, W., Thorne, R. M., & Angelopoulos, V. (2013, May). Global distribution
583 of equatorial magnetosonic waves observed by THEMIS. *Geophys. Res. Lett.*,
584 40, 1895-1901. doi: 10.1002/grl.50434
- 585 Meredith, N. P., Horne, R. B., & Anderson, R. R. (2008, June). Survey of
586 magnetosonic waves and proton ring distributions in the Earth's inner
587 magnetosphere. *J. Geophys. Res. Space Physics*, 113, A06213. doi:
588 10.1029/2007JA012975
- 589 Min, K., & Liu, K. (2016, April). Understanding the growth rate patterns of ion
590 Bernstein instabilities driven by ring-like proton velocity distributions. *J. Geo-*
591 *phys. Res. Space Physics*, 121, 3036-3049. doi: 10.1002/2016JA022524
- 592 Moré, J. J. (1978). The Levenberg-Marquardt algorithm: Implementation and the-
593 ory. In G. A. Watson (Ed.), *Numerical Analysis* (pp. 105-116). Berlin, Heidel-
594 berg: Springer Berlin Heidelberg.
- 595 Němec, F., Parrot, M., & Santolík, O. (2016, October). Equatorial noise emis-
596 sions observed by the DEMETER spacecraft during geomagnetic storms. *J.*
597 *Geophys. Res. Space Physics*, 121, 9744-9757. doi: 10.1002/2016JA023145
- 598 Němec, F., Santolík, O., Parrot, M., & Berthelier, J. J. (2007, April). Comparison of
599 magnetospheric line radiation and power line harmonic radiation: A systematic
600 survey using the DEMETER spacecraft. *J. Geophys. Res. Space Physics*, 112,
601 A04301. doi: 10.1029/2006JA012134
- 602 Němec, F., Santolík, O., Pickett, J. S., Hrbáčková, Z., & Cornilleau-Wehrin, N.
603 (2013, November). Azimuthal directions of equatorial noise propagation de-

- 604 terminated using 10 years of data from the Cluster spacecraft. *J. Geophys. Res.*
 605 *Space Physics*, *118*, 7160-7169. doi: 10.1002/2013JA019373
- 606 Nĕmec, F., Santolík, O., Pickett, J. S., Parrot, M., & Cornilleau-Wehrin, N. (2013,
 607 July). Quasiperiodic emissions observed by the Cluster spacecraft and their as-
 608 sociation with ULF magnetic pulsations. *J. Geophys. Res. Space Physics*, *118*,
 609 4210-4220. doi: 10.1002/jgra.50406
- 610 O'Brien, T. P., & Moldwin, M. B. (2003, February). Empirical plasma-
 611 pause models from magnetic indices. *Geophys. Res. Lett.*, *30*, 1-1. doi:
 612 10.1029/2002GL016007
- 613 Ozhogin, P., Tu, J., Song, P., & Reinisch, B. W. (2012, June). Field-aligned distri-
 614 bution of the plasmaspheric electron density: An empirical model derived from
 615 the IMAGE RPI measurements. *J. Geophys. Res. Space Physics*, *117*, A06225.
 616 doi: 10.1029/2011JA017330
- 617 Parrot, M., Benoist, D., Berthelier, J. J., Błęcki, J., Chapuis, Y., Colin, F., ...
 618 Zamora, P. (2006, April). The magnetic field experiment IMSC and its data
 619 processing onboard DEMETER: Scientific objectives, description and first
 620 results. *Planet. Space Sci.*, *54*, 441-455. doi: 10.1016/j.pss.2005.10.015
- 621 Perraut, S., Roux, A., Robert, P., Gendrin, R., Sauvaud, J. A., Bosqued, J. M., ...
 622 Korth, A. (1982, August). A systematic study of ULF waves above F_{H+} from
 623 GEOS 1 and 2 measurements and their relationships with proton ring distribu-
 624 tions. *J. Geophys. Res.*, *87*, 6219-6236. doi: 10.1029/JA087iA08p06219
- 625 Posch, J. L., Engebretson, M. J., Olson, C. N., Thaller, S. A., Breneman, A. W.,
 626 Wygant, J. R., ... Reeves, G. D. (2015, August). Low-harmonic magnetosonic
 627 waves observed by the Van Allen Probes. *J. Geophys. Res. Space Physics*,
 628 *120*(8), 6230-6257. doi: 10.1002/2015JA021179
- 629 Russell, C. T., Holzer, R. E., & Smith, E. J. (1970, January). OGO 3 observations
 630 of ELF noise in the magnetosphere: 2. The nature of the equatorial noise. *J.*
 631 *Geophys. Res.*, *75*, 755. doi: 10.1029/JA075i004p00755
- 632 Santolík, O., Nĕmec, F., Gereová, K., Macúšová, E., Conchy, Y., & Cornilleau-
 633 Wehrin, N. (2004, July). Systematic analysis of equatorial noise be-
 634 low the lower hybrid frequency. *Ann. Geophys.*, *22*, 2587-2595. doi:
 635 10.5194/angeo-22-2587-2004
- 636 Santolík, O., Nĕmec, F., Parrot, M., Lagoutte, D., Madrias, L., & Berthelier, J. J.

- 637 (2006, April). Analysis methods for multi-component wave measurements
 638 on board the DEMETER spacecraft. *Planet. Space Sci.*, *54*, 512-527. doi:
 639 10.1016/j.pss.2005.10.020
- 640 Santolík, O., Parrot, M., Inan, U. S., Burešová, D., Gurnett, D. A., & Chum, J.
 641 (2009, March). Propagation of unducted whistlers from their source light-
 642 ning: A case study. *J. Geophys. Res. Space Physics*, *114*, A03212. doi:
 643 10.1029/2008JA013776
- 644 Santolík, O., Parrot, M., & Lefeuvre, F. (2003, February). Singular value decomposi-
 645 tion methods for wave propagation analysis. *Rad. Sci.*, *38*, 10-1. doi: 10.1029/
 646 2000RS002523
- 647 Santolík, O., Parrot, M., & Němec, F. (2016, July). Propagation of equatorial noise
 648 to low altitudes: Decoupling from the magnetosonic mode. *Geophys. Res. Lett.*,
 649 *43*, 6694-6704. doi: 10.1002/2016GL069582
- 650 Santolík, O., Pickett, J. S., Gurnett, D. A., Maksimovic, M., & Cornilleau-Wehrin,
 651 N. (2002, December). Spatiotemporal variability and propagation of equatorial
 652 noise observed by Cluster. *J. Geophys. Res. Space Physics*, *107*(A12), 1495.
 653 doi: 10.1029/2001JA009159
- 654 Santolík, O., Pickett, J. S., Gurnett, D. A., Menietti, J. D., Tsurutani, B. T., &
 655 Verkhoglyadova, O. (2010, July). Survey of Poynting flux of whistler mode
 656 chorus in the outer zone. *J. Geophys. Res. Space Physics*, *115*, A00F13. doi:
 657 10.1029/2009JA014925
- 658 Santolík, O., Pickett, J. S., Gurnett, D. A., & Storey, L. R. O. (2002, Dec). Mag-
 659 netic component of narrowband ion cyclotron waves in the auroral zone. *J.*
 660 *Geophys. Res. Space Physics*, *107*(A12), 1444. doi: 10.1029/2001JA000146
- 661 Stix, T. (1992). *Waves in Plasmas*. Melville NY: American Institute of Physics.
- 662 Tsyganenko, N. A. (1989, January). A magnetospheric magnetic field model with
 663 a warped tail current sheet. *Planet. Space Sci.*, *37*, 5-20. doi: 10.1016/0032-
 664 -0633(89)90066-4
- 665 Xiao, F., Zhou, Q., He, Z., Yang, C., He, Y., & Tang, L. (2013, July). Magnetosonic
 666 wave instability by proton ring distributions: Simultaneous data and modeling.
 667 *J. Geophys. Res. Space Physics*, *118*, 4053-4058. doi: 10.1002/jgra.50401